The Astrophysical Journal, 928:49 (16pp), 2022 March 20 https://doi.org/10.3847/1538-4357/ac5111

ALMA High-resolution Multiband Analysis for the Protoplanetary Disk around TW Hya

Takashi Tsukagoshi[1], Hideko Nomura[1], Takayuki Muto[2], Ryohei Kawabe[1], Kazuhiro D. Kanagawa[3], Satoshi Okuzumi[4], Shigeru Ida[5], Catherine Walsh[6], Tom J. Millar[7], Sanemichi Z. Takahashi[1], Jun Hashimoto[8], Taichi Uyama[9,10], and Motohide Tamura[8,11,12]
[1] Division of Science, National Astronomical Observatory of Japan, Osawa 2-21-1, Mitaka, Tokyo 181-8588, Japan; takashi.tsukagoshi.astro@gmail.com
[2] Division of Liberal Arts, Kogakuin University, 1-24-2 Nishi-Shinjuku, Shinjuku-ku, Tokyo 163-8677, Japan
[3] College of Science, Ibaraki University, Bunkyo 2-1-1, Mito, Ibaraki, 310-8512, Japan
[4] Department of Earth and Planetary Sciences, Tokyo Institute of Technology, 2-12-1 Ookayama, Meguro, Tokyo 152-8551, Japan
[5] Earth-Life Science Institute, Tokyo Institute of Technology, 2-12-1 Ookayama, Meguro, Tokyo 152-8550, Japan
[6] School of Physics and Astronomy, University of Leeds, Leeds, LS2 9JT, UK
[7] Astrophysics Research Centre, School of Mathematics and Physics, Queen's University Belfast, University Road, Belfast, BT7 1NN, UK
[8] Astrobiology Center, 2-21-1 Osawa, Mitaka, Tokyo 181-8588, Japan
[9] Infrared Processing and Analysis Center, California Institute of Technology, Pasadena, CA 91125, USA
[10] NASA Exoplanet Science Institute, California Institute of Technology, Pasadena, CA 91125, USA
[11] Subaru Telescope, National Astronomical Observatory of Japan, Osawa 2-21-1, Mitaka, Tokyo 181-8588, Japan
[12] Department of Astronomy, School of Science, University of Tokyo, Bunkyo, Tokyo 113-0033, Japan
Received 2021 March 15; revised 2022 January 28; accepted 2022 January 31; published 2022 March 25

Abstract

We present a high-resolution (2.5 au) multiband analysis of the protoplanetary disk around TW Hya using Atacama Large Millimeter/submillimeter Array (ALMA) long baseline data at Bands 3, 4, 6, and 7. We aim to reconstruct a high-sensitivity millimeter continuum image and revisit the spectral index distribution. The imaging is performed by combining new ALMA data at Bands 4 and 6 with available archive data. Two methods are employed to reconstruct the images: multifrequency synthesis (MFS) and the fiducial image-oriented method, where each band is imaged separately and the frequency dependence is fitted pixel by pixel. We find that MFS imaging with a second-order Taylor expansion can reproduce the frequency dependence of the continuum emission between Bands 3 and 7 in a manner consistent with previous studies, and that it is a reasonable method for reconstructing the spectral index map. The image-oriented method provides a spectral index map consistent with the MFS imaging, but with a two times lower resolution. Mock observations of an intensity model were conducted to validate the images from the two methods. We find that the MFS imaging provides a high-resolution spectral index distribution with an uncertainty of $<10\%$. Using the submillimeter spectrum reproduced from our MFS images, we directly calculate the optical depth, power-law index of the dust opacity coefficient (β), and dust temperature. The derived parameters are consistent with previous works, and the enhancement of β within the intensity gaps is also confirmed, supporting a deficit of millimeter-sized grains within the gaps.

Unified Astronomy Thesaurus concepts: Protoplanetary disks (1300); Submillimeter astronomy (1647); Planet formation (1241)

1. Introduction

Protoplanetary disks surrounding young stars are the birthplaces of planets. Forming planets are thought to interact with the parent protoplanetary disk and cause various substructures, such as an inner hole, gaps and rings, and large-scale asymmetries. High-resolution observations with radio interferometers, such as the Atacama Large Millimeter/submillimeter Array (ALMA), have revealed that dust substructures within protoplanetary disks are common and are rich in variety (e.g., Andrews et al. 2018). Recent high-resolution ALMA observations with deep integrations have revealed au-scale dust substructures that may be caused by a forming planet and a surrounding circumplanetary disk (Isella et al. 2019; Tsukagoshi et al. 2019). Further observational constraints are essential for confirming the physical origins of these substructures.

The first steps toward the formation of a planet involve the coagulation and growth of dust grains. Hence, revealing the evolution of dust grains in protoplanetary disks is key to understanding the origin and diversity of planetary systems, and placing observational constraints on the dust size distribution is crucial. Theoretical models of dust transport, fragmentation, and size evolution predict that the average size of a grain varies with disk radius (Dullemond & Dominik 2005). The picture of dust filtration by a forming planet in a protoplanetary disk assumes that a planet-induced gap filters large dust grains at the outer edge of the gap, while the remaining small grains pass across the gap (Zhu et al. 2012). It is also suggested that the maximum grain size should be smaller by a factor of 100 inside the condensation front of water ice, i.e., the H_2O snow line (Banzatti et al. 2015). Because the H_2O snow line may be a boundary that determines the type of planet formed (e.g., terrestrial planets, gas giants, or icy giants; Hayashi 1981), it is important to reveal the position of the snow line in the protoplanetary disk to understand the planetary formation process.

Multifrequency observations at (sub)millimeter wavelengths are an effective way of measuring the dust size distribution and obtaining a high-sensitivity intensity image by increasing the

total bandwidth. The dust size distribution can be inferred by measuring the spectral index α at (sub)millimeter frequencies. When the dust continuum emission at (sub)millimeter frequencies is optically thin, the frequency dependence of the dust mass opacity coefficient κ_ν is evident in the α profile. The dust mass opacity coefficient is often described as having a power-law form ($\kappa_\nu \propto \nu^\beta$), and in the Rayleigh–Jeans limit β is related to α as $\beta = \alpha - 2$. It is known that β is affected by the dust size; $\beta \sim 1.7$ for sub-micron-sized interstellar grains, while it changes to $\beta \sim 1$ or less owing to grain growth in protoplanetary disks (e.g., Miyake & Nakagawa 1993). Therefore, multifrequency observations at optically thin (sub) millimeter wavelengths are essential for revealing the dust size distribution of the disk.

High-resolution multifrequency observations with ALMA have been conducted on protoplanetary disks to resolve the radial dependence of the dust size distribution (e.g., ALMA Partnership et al. 2015; Dent et al. 2019; Huang et al. 2020; Long et al. 2020). There are several ways to concatenate multifrequency data for imaging the combined intensity and producing the spectral index maps. The first is an image-oriented method. This is the traditional method, in which the intensity map at each band is created separately and the frequency dependence is fitted pixel by pixel using a power-law function. This method requires matching the beam sizes across all of the images before the fitting. Another method of concatenating multifrequency data is multiscale multifrequency synthesis (MFS), introduced by Rau & Cornwell (2011), in which all of the observed visibilities are concatenated to simultaneously create combined intensity and spectral index maps. This operation can provide higher-resolution maps than those of the image-oriented method. Rau & Cornwell (2011) demonstrated that MFS works well for the imaging of a compact, flat-spectrum source at lower frequencies ($\sim$1 GHz), motivated by the application to synchrotron emission. The authors pointed out that the UV coverage has a significant impact on reconstructing the spectral index map of spatially extended emission. On the other hand, the thermal continuum emission within the dust of a protoplanetary disk has a spectral slope α of 2–4, depending on the optical depth and dust mass opacity coefficient. In addition, recent high-resolution observations have revealed that the disks are often spatially extended. Therefore, it is worth validating whether MFS works well for reconstructing the (sub)millimeter continuum emission of a protoplanetary disk and its frequency dependence.

TW Hya is a 0.8 $M_\odot$ T Tauri star surrounded by a gas-rich protoplanetary disk at a distance of 59.5 pc (e.g., Gaia Collaboration et al. 2016). The disk is almost face-on, with an inclination angle of 5°–6° (Huang et al. 2018; Teague et al. 2019); thus, it is one of the best targets for investigating the radial structure of a protoplanetary disk. The disk has been well resolved at (sub)millimeter, near-infrared, and optical wavelengths. Multiple gap structures in the near-infrared scattered light have been reported (Akiyama et al. 2015; van Boekel et al. 2017). ALMA has also resolved gaps at (sub)millimeter wavelengths, and an inner disk with a size of $\sim$1 au has also been identified (Andrews et al. 2016; Tsukagoshi et al. 2016; Huang et al. 2018). The features detected thus far within the protoplanetary disk are almost axisymmetric, except for a moving surface brightness asymmetry, probably due to a disk shadow (Debes et al. 2017) and a spiral pattern found in the CO gas (Teague et al. 2019). Another asymmetric structure of the disk is a localized compact ($\sim$1 au) excess emission at millimeter wavelengths near the edge of the dust disk identified in high-sensitivity ALMA observations (Tsukagoshi et al. 2019). The origin of the emission feature remains unclear, but it may be caused by a circumplanetary disk surrounding a Neptune-mass planet or dust grains accumulated within a small-scale gas vortex. According to a recent theoretical study, the emission feature could also be a dust-losing young planet that has already been formed (Nayakshin et al. 2020).

The dust size distribution of the TW Hya disk has been inferred using high-resolution multifrequency observations with ALMA (Tsukagoshi et al. 2016; Huang et al. 2018). The observations have revealed that the spectral index α decreases toward the disk center, and there is an enhancement near the gap at 25 au. This enhancement may be attributed to the dust filtration effect, in which the gap is deficient in large grains (Zhu et al. 2012). However, there is still uncertainty on the radial variation of the α profile. The UV sampling of our previous observations in 2015 was particularly sparse at $<$200 kλ, and the integration time was as short as $\lesssim$40 minutes (Tsukagoshi et al. 2016). Hence, the poorly sampled UV coverage makes image reconstruction difficult, because the synthesized beam shows a complicated sidelobe pattern. This caused difficulties in the image reconstruction by CLEAN, which highly depends on the imaging parameters, such as the weighting and the scale parameters of multiscale cleaning. Additional uncertainty arises from adopting only two ALMA bands to derive the spectral index. A combination of more than two bands can better constrain the spectral index by improving the frequency leverage. Most recently, Macias et al. (2021) presented an analysis of the spectral index distribution of TW Hya's disk using sets of high-resolution ALMA data from Bands 3 to 7, and the variation of the spectral index within the analyzed frequency range was reported. As they focused on the spectral indices between two adjacent bands, a high-sensitivity continuum image integrated over all of the bands was not presented.

In this study, we attempt to reconstruct a higher-sensitivity millimeter continuum image and revisit the spectral index distribution of the TW Hya disk using multiple sets of ALMA data at Bands 3, 4, 6, and 7. Two imaging methods, MFS and the image-oriented method, are adopted to combine all of the data and to derive the spectral index map. The details of the observations and data reduction are presented in Section 2. In Section 3, the images of the combined intensity and spectral index are shown, and we compare them from the viewpoints of the different imaging methods. To validate our reconstructed images, we test the imaging methods using simulations with a disk model in Section 4. In Section 5, we compare our results with the recent high-resolution spectral index profiles presented by Macias et al. (2021). We also discuss the dust size distribution in the disk by deriving the distribution of the optical depth τ, the power-law index of the dust mass opacity coefficient β, and the dust temperature T_d. Lastly, we present a summary of this paper in Section 6.

2. Observations and Data Reduction

In this study, we use sets of ALMA archive data at Bands 3, 4, 6, and 7 to reconstruct a high-sensitivity combined intensity map and a spectral index map covering these frequencies. Here, we describe the details of our observations and data reduction. The Band 4 and 6 data include our new observations, and the

Table 1
ALMA Data Employed in This Study

ID	PI	Date	Configuration	L_{min} (m)	L_{max} (m)	t_{integ} (minutes)	B_{total} (MHz)	CASA Ver.
			Band 3					
2016.1.00229.S	Bergin, E.	2017 Aug 1	C40-7	17	149	41	2293	4.7.2
2018.1.01218.S	Macias, E.	2019 Jun 24–Jul 8	C43-9/10	149	16196	209	7500	5.4.0
			Band 4					
2015.A.00005.S	Tsukagoshi, T.	2015 Dec 2	C36-8/7	17	10803	43	7500	4.5.0
2015.1.00845.S	Favre, C.	2016 Apr 29	C36-2/3	15	640	80	3750	4.5.3
2015.1.00845.S	Favre, C.	2016 Jun 1	C40-4	15	713	76	1875	4.5.3
2016.1.00842.S	Tsukagoshi, T.	2017 Sep 28	C40-6	19	1808	37	7500	4.7.0
2016.1.00842.S	Tsukagoshi, T.	2016 Oct 21	C40-8/9	41	14851	23	7500	4.7.2
2016.1.00440.S	Teague, R.	2016 Oct 22	C40-6	19	1400	141	1875	4.7.0
			Band 6					
2013.1.00387.S	Guilloteau, S.	2015 May 13	C34-3	21	558	47	1875	4.2.2
2013.1.00114.S	Ob¨erg, K.	2014 Jul 19	C34-4/5	34	650	43	938	4.2.2
2015.A.00005.S	Tsukagoshi, T.	2015 Dec 2	C36-8/7	17	10803	40	7500	4.5.0
2016.1.00842.S	Tsukagoshi, T.	2017 May 15	C40-5	15	1121	11	7500	4.7.2
2017.1.00520.S	Tsukagoshi, T.	2017 Nov 20	C43-8	92	8548	118	7500	5.1.1
			Band 7					
2015.1.00686.S	Andrews, S.	2015 Nov 23	C36-8/7	17	14238	132	6094	4.5.0
2015.1.00308.S	Bergin, E.	2016 Mar 8	C36-3	15	460	69	3750	4.5.2
2016.1.00229.S	Bergin, E.	2016 Nov 23	C40-4	15	704	49	3281	4.7.0
2016.1.00440.S	Teague, R.	2016 Nov 27	C40-3	15	704	48	1172	4.7.2
2016.1.00464.S	Walsh, C.	2016 Dec 3	C40-4	15	704	342	1875	4.7.2
2016.1.01495.S	Nomura, H.	2016 Dec 6	C40-3	15	704	43	1172	4.7.0
2016.1.00629.S	Cleeves, I.	2016 Dec 30	C40-3	15	460	84	2578	4.7.0
2016.1.00311.S	Cleeves, I.	2017 May 21	C40-5	15	390	48	1875	4.7.2

details of the observations are described in the following subsections. All of the ALMA measurement sets were reduced and calibrated using the Common Astronomical Software Application (CASA) package (McMullin et al. 2007). The data IDs used in this study and their detailed information are listed in Table 1. Figure 1 shows the achieved UV coverage of each band's combined data. The method for obtaining the combined intensity and spectral index maps is also described in the following subsection.

2.1. Band 3 Data

We have used archival data from two ALMA projects that were recently published by Macias et al. (2021). The details of the archive data and the CASA versions used for the pipeline analysis are listed in Table 1. The pipeline script provided by ALMA was used for the initial data flagging and the calibration of the bandpass characteristics and the complex gain. To concatenate the data obtained at different epochs, we first created a dirty map of each data set to determine the representative position of the emission, i.e., the center of the disk emission. The dirty map was reconstructed with Briggs weighting with a robust parameter of 0.5, and the position of the emission peak was measured by a 2D Gaussian fitting to the emission using CASA *imfit*. Subsequently, the field center of each measurement set was corrected to be the disk center by CASA *fixvis*. Then, all of the measurement sets were concatenated by CASA *concat* with a direction shift tolerance towards a single field center for correcting the proper motion of the source.

The concatenated visibilities were imaged using the CASA *tclean* task. The CLEAN map was reconstructed by adopting the Briggs weighting with a robust parameter of 0.5. We also employed the multiscale CLEAN algorithm with scale parameters of [0, 50, 150] mas. After the initial CLEAN map was reconstructed, we applied phase self-calibration to the concatenated data. We adopted solution intervals varying from 1200 to 60 s for the shorter baseline data and from 6000 to 900 s for the longer baseline data. The self-calibration started from longer solution intervals than the target scan to remove the systematic phase offsets between the concatenated measurement sets. Then, the self-calibration was stopped at the shortest solution interval where the signal-to-noise ratio (S/N) was enough to solve above 2σ, i.e., only a small number of visibilities were flagged out. After the phase self-calibration was done, one round of amplitude self-calibration was applied with a solution interval for each observation period. However, the image sensitivity was less affected by self-calibration, so that the noise level of the final CLEAN map was 4.3 μJy beam^{-1}. The beam size was 53.0×50.7 mas, with a position angle of $-7\overset{\circ}{.}7$.

2.2. Band 4 Data

Our ALMA Band 4 observations (2016.1.00842.S) were conducted on 2016 September 28, with array configuration C40-9, and on 2016 October 21, with C40-6. The total integration times were 12 minutes and 38 minutes, respectively. In addition to the observed data set, we employed ALMA archive data (2015.A.00005.S, 2015.1.00845.S, and

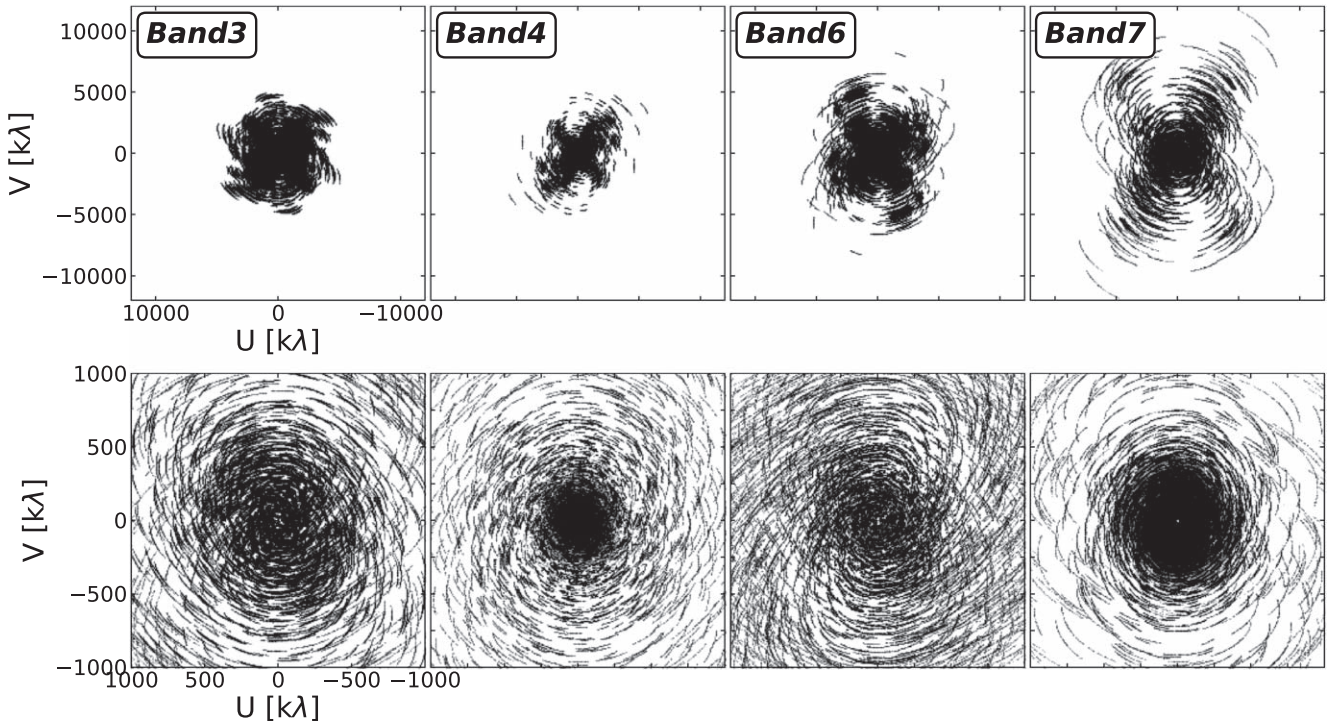

Figure 1. Whole view of the UV coverage of the combined data of Bands 3, 4, 6, and 7, from left to right (top). Close-up view of the UV coverage inside ±1000 kλ (bottom).

2016.1.00440.S) and concatenated them to obtain better sensitivity and UV coverage.

The initial flagging and calibrations were performed by using the pipeline scripts, and the calibrated visibilities were concatenated using the same procedure as for the Band 3 data. The CLEAN map of the combined measurement set was reconstructed by adopting Briggs weighting with a robust parameter of 0. We employed a multiscale option with scale parameters of [0, 50, 150] mas. The self-calibration in phase was applied with solution intervals of 3600, 900, 300, and 150 s, and followed by the amplitude self-calibration with the intervals of each observation period. The spatial resolution of the final CLEAN map at Band 4 was 85.1 × 50.4 mas, with a position angle of 45°.4, and the noise level of the self-calibrated CLEAN map was 7.8 μJy beam^{-1}.

2.3. Band 6 Data

Our Band 6 observations were carried out on 2017 May 15, with array configuration C40-5 (2016.1.00842.S), and in the period from 2017 November 20 to 25, with C43-8 (2017.1.00520.S), during ALMA cycles 3 and 4. A description of the observations and the obtained image has already been published (Tsukagoshi et al. 2019). To improve the sensitivity, we obtained archive data 2013.1.00114.S, 2013.1.00387.S, and 2015.A.00005.S and concatenated them with the observed data to create the final Band 6 image.

After the initial data flagging and calibrations using the pipeline script, the same procedure as for the Band 3 data was applied to concatenate the calibrated measurement sets. The imaging procedure was the same as that for the Band 3 data, except for some imaging parameters. The CLEAN map was reconstructed using Briggs weighting with a robust parameter of 0.5. The scale parameters for the multiscale CLEAN were set to [0, 42, 126] mas. The phase-only self-calibration was applied by varying the solution interval from 3600 to 120 s, and was followed by the amplitude self-calibration. The noise level of the final CLEAN image was 8.1 μJy beam^{-1}. The beam size of the final image was 46.9 × 40.6 mas, with a position angle of 86°.4.

2.4. Band 7 Data

To create a high-resolution Band 7 image, we have used eight sets of ALMA archive data, presented in Tsukagoshi et al. (2019), including the highest-resolution data obtained by Andrews et al. (2016). The data reduction and imaging was performed with the same procedure as for the other bands, except for some imaging parameters. We employed the Briggs weighting with a robust −1.0 for reconstructing the CLEAN map. The phase-only self-calibration was applied by varying the solution interval from 7200 to 1200 s. With the phase-only self-calibration, the image noise level was improved from 124 to 32.8 μJy beam^{-1}, corresponding to an improvement in the S/N from ∼18 to ∼62. Then, the amplitude self-calibration was performed with a solution interval of each observation period. The noise level and beam size of the final CLEAN image were 21.8 μJy beam^{-1} and 36.4 × 28.9 mas, with a position angle of 69°.9, respectively. The details of the data reduction have also been described in Tsukagoshi et al. (2019).

2.5. Reconstruction of the Intensity and Spectral Index Maps from All Band Data

To combine the entire data set from Bands 3 to 7, we first corrected the proper motion by aligning the field center in the same manner for the data from each band. The disk center was derived by 2D Gaussian fitting to the bright part of the emission in the CLEAN map of each band. The field center of the

measurement set at each band was updated to be the disk center. Then, all of the measurement sets were concatenated using *concat*, with the direction tolerance being a single field. With this concatenated measurement set, we reconstructed the intensity and spectral index maps at the central frequency using the two methods described in the following subsections. To match the minimum and maximum UV lengths between the data from all bands, we employed the data in the baseline range of 14–5100 kλ. We used CASA version 6.2 for reconstructing the images.

2.5.1. Image-oriented Method

Before making the maps, the concatenated measurement set was first divided into each band, and CLEAN images were made with Briggs weighting with a robust parameter of 0. We employed the same image size and cell size to directly apply the mathematical operation to the images. The multiscale CLEAN algorithm was also employed, with scales of 0, 54, and 162 mas. All of the reconstructed CLEAN images were convolved to have a circular beam with an FWHM of 108 mas ($\sim$6.4 au), which is the largest beam major axis among the CLEAN images.

For each pixel in the convolved images, we fit a power-law function $I = I_0(\nu/\nu_0)^{I_\alpha}$ along the frequency axis. Here, I_0 is the intensity at the central frequency $\nu_0 = 221$ GHz. Note that image pixels where the emission is higher than 5σ are used for the fit. The noise levels of the CLEAN maps are 4.3, 9.4, 13, and 49 μJy beam^{-1} for Bands 3, 4, 6, and 7, respectively. The fitting was performed using *curve_fit* in the *scipy* package[13] (Virtanen et al. 2020).

According to the ALMA proposer's guide, the uncertainties of the absolute flux calibration of ALMA are 5%, 5%, 10%, and 10% for Bands 3, 4, 6, and 7, respectively. This corresponds to the fitting error of the spectral index with the image-oriented method being less than 0.01. Note that the uncertainty of the absolute flux calibration is lower than the above value because we combine some measurement sets for each band.

2.5.2. Multiscale and Multifrequency Synthesis

To create the combined intensity and spectral index maps, we also employed a multiscale MFS method implemented in the CASA *tclean* task (deconvolver = mtmfs; Rau & Cornwell 2011). In this method, the images are reconstructed by simultaneously solving the CLEAN components in the spatial and spectral regimes. In particular, the MFS method solves the frequency dependence of the intensity by adopting the Taylor expansion of the following equations:

$$I_\nu = I_{\nu_0}\left(\frac{\nu}{\nu_0}\right)^{I_\alpha + I_\beta \log\left(\frac{\nu}{\nu_0}\right)} \quad (1)$$

$$\sim I_0 + I_1\left(\frac{\nu-\nu_0}{\nu_0}\right) + I_2\left(\frac{\nu-\nu_0}{\nu_0}\right)^2 + ... \quad (2)$$

Here, I_{ν_0} is the intensity value at the representative frequency ν_0, and I_α and I_β are the values of the power-law index and the curvature of the frequency dependence, respectively. The Taylor coefficients I_n ($n = 0, 1, 2, ...$) were determined via the deconvolution process. If we take the first order of the Taylor expansion, the first two coefficients I_0 and I_1 correspond to $I_0 = I_{\nu_0}$ and $I_1 = I_\alpha I_{\nu_0}$, and thus I_{ν_0} and I_α can be calculated from the coefficients. For the second order of the Taylor expansion, I_β can be obtained using the third coefficient:

$$I_2 = \left(\frac{I_\alpha(I_\alpha - 1)}{2} + I_\beta\right) I_{\nu_0}. \quad (3)$$

The polynomial approximation of the power-law function is a source of errors. Although increasing the number of Taylor terms would be better for reproducing the power-law dependence of the frequencies, the use of too many terms could increase the critical errors for noisy data, because of the increasing number of free parameters. In addition, the total frequency coverage of the available images with respect to the representative frequency, i.e., the bandwidth ratio, could be a source of errors. This is because the wider the bandwidth, the more Taylor terms are required to reproduce the power-law dependence.

The concatenated measurement set with data from all bands was imaged by adopting the *mtmfs* option in *tclean*, in which the number of Taylor coefficients is controlled by the *nterms* parameter; *nterms* = 2 and *nterms* = 3 mean that the frequency dependence is described by the Taylor expansion to the first and second orders, respectively. We created maps with *nterms* = 2, 3, and 4 because the frequency range is wide, with a value of 95–360 GHz. The combined intensity map at a central frequency of 221 GHz and the spectral index map were reconstructed from all of the calibrated visibilities using Briggs weighting with a robust parameter of 0. The scale parameter of the multiscale CLEAN was set to [0, 54, 162] mas. The resolution of the final images was 46.0×42.5 mas, with a position angle of 42°.3. Note that the uncertainty in the spectral index measurement with this method due to the absolute flux calibration is estimated to be less than 8% from mock observations with an intensity model. Moreover, the uncertainty does not affect the shape of the I_α profile, but the entire profile was scaled. See Section 4 for more details.

3. Results

Figure 2 (top) shows the intensity map at the central frequency (221 GHz) I_0 and the spectral index map I_α obtained using the image-oriented method. Although the beam size is almost double that of previous studies (Andrews et al. 2016; Tsukagoshi et al. 2016; Huang et al. 2018), the combined intensity map resolves the disk substructures, two clear gaps and an inner hole, as shown in the leftmost panel of Figure 2 (top). The total flux density integrated over the disk emission is estimated to be 403 mJy. The spectral index map shows the radial variation as previously reported (Tsukagoshi et al. 2016; Huang et al. 2018). The spectral index is $\sim$3.0 near the outermost disk, and decreases to less than 2 inside 20 au. There are enhancements of the spectral index that are likely associated with the gaps in the intensity distribution at 25 and 42 au. The rightmost panel of Figure 2 (top) shows the deprojected radial profiles of the intensity and the spectral index maps. The error bars are determined by the standard error through azimuthal averaging. Note that for the deprojection, we employed an inclination of 7° (Qi et al. 2004), which is 1°–2° larger than that determined by recent works (Huang et al. 2018;

[13] https://scipy.org

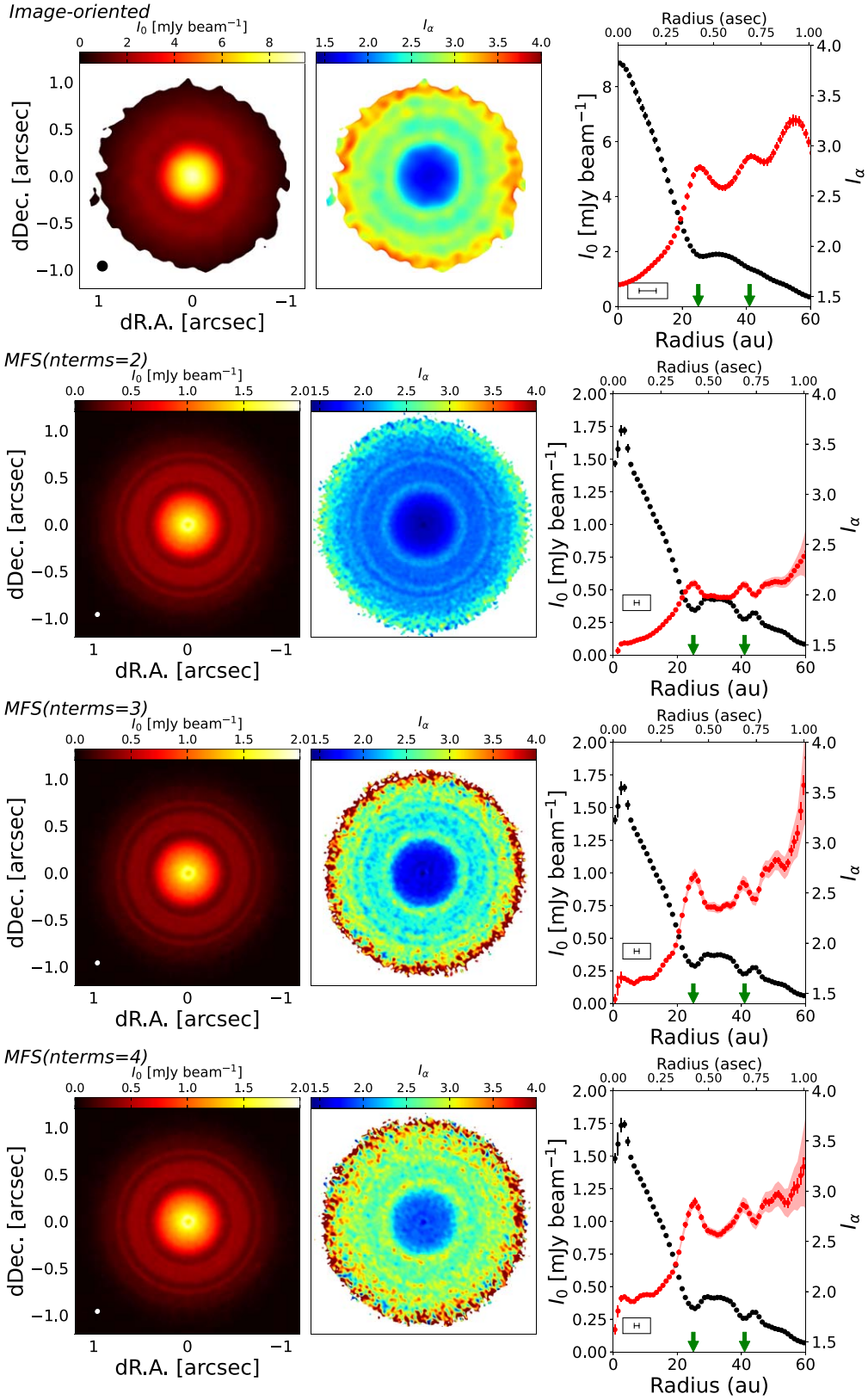

Figure 2. Combined intensity (left) and spectral index I_α (center) maps. The circle in the bottom left corner of the intensity panel shows the beam size. The right-hand panel shows the radial profiles of the intensity (black) and I_α (red) azimuthally averaged after the image deprojection. The error bars show the standard error through azimuthal averaging. The shaded region indicates the value of the I_α error map that CASA *tclean* provided. The bar in the bottom left corner denotes the geometric mean of the beam size. The images reconstructed by the image-oriented analysis are shown in the top row, and those reconstructed by MFS are shown from the second to bottom rows. The noise of the intensity map of the image-oriented method is 95 μJy beam^{-1}, and that of the MFS maps for *nterms* = 2–4 is 7.5 μJy beam^{-1}. The green arrows in the right-hand panels indicate the positions of the 25 and 41 au gaps, respectively.

Teague et al. 2019). This slight difference does not affect the profiles.

The I_0 and I_α maps reconstructed using MFS are also shown in Figure 2 (second to bottom rows). The deprojected radial profiles are also shown in the right-hand panels of the figure. The shaded region of the I_α profile shows the I_α error map, which is the outcome of CASA *tclean* with the *mtmfs* option. Evidently, with the higher spatial resolution of MFS than that of the image-oriented method, the I_0 map shows the disk substructures more clearly. The intensity maps reconstructed with different *nterms* show no clear difference. The image noise level of the maps is 7.5 μJy beam^{-1}. The peak intensities are 1.79, 1.73, and 1.83 mJy beam^{-1}, and the total flux densities are 526, 471, and 549 mJy for *nterms* = 2, 3, and 4, respectively. There is a slight difference in the measured flux densities, but it is less than 10%.

The shape of the I_α profile reconstructed by MFS with *nterms* = 2 is similar to that of the image-oriented method. Starting from the outermost part, I_α gradually decreases toward ~25 au, with slight enhancements associated with the intensity gaps, then suddenly drops near 20 au, and has a lower value in the innermost region. However, the absolute value of I_α reconstructed with *nterms* = 2 is much smaller than that of the image-oriented method.

In contrast to the *nterms* = 2 case, the absolute value of I_α is similar to that for the *nterms* = 3 and 4 cases. Both cases show a similar I_α profile, varying from ~3 to $\lesssim$2 toward the disk center, whereas there is a slight difference between them (~0.3). The I_α enhancements at the gaps are also observed to have similar values to the image-oriented case.

To determine how the order of the Taylor expansion reproduces the power-law dependence across the observed frequencies, we performed a least-squares fitting of the first and second orders of the Taylor expansion of a power-law function to a model spectrum with $I_\nu \propto \nu^{2.5}$ sampled at the observed frequencies. A pure power-law function was also employed for the fitting as a reference. The results of the fitting are shown in Figure 3. As mentioned previously, the first order of the Taylor expansion (*nterms* = 2) is insufficient to reproduce the power-law form of the submillimeter spectrum between the observed bands. In contrast, the second order of the Taylor expansion can almost reproduce the power-law dependence. This indicates that at least the second order of the Taylor expansion is required to measure the spectral index between the observed bands with MFS.

If we adopt *nterms* = 3 and 4, we can obtain a map showing the spectral curvature I_β (Equation (3)), as shown in Figure 4. The maps of the spectral curvatures I_β and their deprojected profiles clearly show that I_β varies with radius for both cases. Nonzero I_β implies a frequency dependence in the spectral slope within the observed bands. There is a difference in the value of I_β between the *nterms* = 3 and 4 cases. For *nterms* = 3, I_β is ~0 near the disk center, and gradually decreases to −1.0 toward the outer disk, with a slight variation in the intensity gaps. This indicates that, in almost all regions of the disk, the spectral index decreases as the frequency increases. The positive I_β at the innermost part of the disk implies the opposite trend of the spectral index, which is consistent with the existence of free–free emission at the stellar position suggested in previous studies (Pascucci et al. 2012; Macias et al. 2021). On the other hand, for *nterms* = 4, I_β is from −1.0 to −0.5 near the disk center, and drastically decreases to

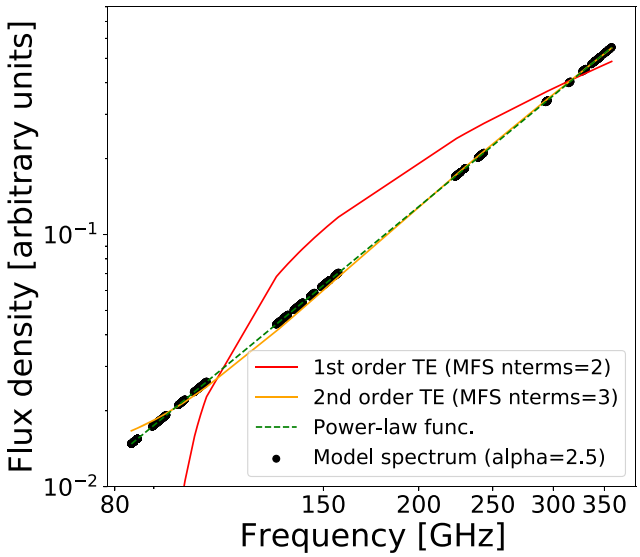

Figure 3. The reproducibility of the submillimeter spectrum for different *nterms*. The flux densities are determined to follow a power-law index of 2.5, and the spectrum is sampled at the frequencies of the observation data. The solid lines show the fit using the equations for *nterms* = 2 (red) and *nterms* = 3 (yellow), while the fit using a power-law function is shown by the dotted line in green. The vertical axis shows the flux density in arbitrary units. "TE" is an abbreviation of Taylor expansion.

~−1.7 at ~20 au. The relatively large error bars of I_β for the *nterms* = 4 case are probably because a larger number of Taylor coefficients must be determined for higher orders of the Taylor expansion. The submillimeter spectrum inferred from the I_α and I_β profiles using Equation (1) is also shown in Figure 4. When comparing the flux densities of each band, it is clear that the combination of I_α and I_β for the *nterms* = 3 case reproduces the observed submillimeter spectrum better than the *nterms* = 4 case. This difference is due to the number of Taylor terms used to describe the submillimeter spectrum. In MFS, the submillimeter spectrum is described by Equation (1) using three imaging parameters, I_0, I_α, and I_β, and they are calculated using the first three Taylor coefficients, I_0, I_1, and I_2. With MFS *nterms* = 3, the spectrum is described with the first three Taylor coefficients, and thus it is preferable because the parameters of the spectrum can be determined uniquely. For *nterms* = 4, on the other hand, we obtain four Taylor coefficients from the MFS imaging. However, the final Taylor term is not employed for the spectrum calculation, though it is nonzero. This likely causes a difference between the calculated spectrum and the observed flux density for the case of *nterms* = 4.

The point-source sensitivity of our millimeter continuum image reconstructed with MFS is improved by ~30% from the deepest image so far for TW Hya at high resolution (<50 mas) by Tsukagoshi et al. (2019). The high-resolution and high-sensitivity continuum map reconstructed with MFS provides an opportunity to search for substructures associated with the millimeter blob located at 52 au, as found by Tsukagoshi et al. (2019). Figure 5 shows the intensity map of MFS *nterms* = 3 deprojected into a map in polar coordinates, whose intensity scale is normalized by an exponential function (see Section 4) to more easily identify substructures. We tentatively find an emission feature that could be a trailing tail that has emerged from the millimeter blob (Nayakshin et al. 2020). However, it is also possible that the emission feature is an artifact caused by

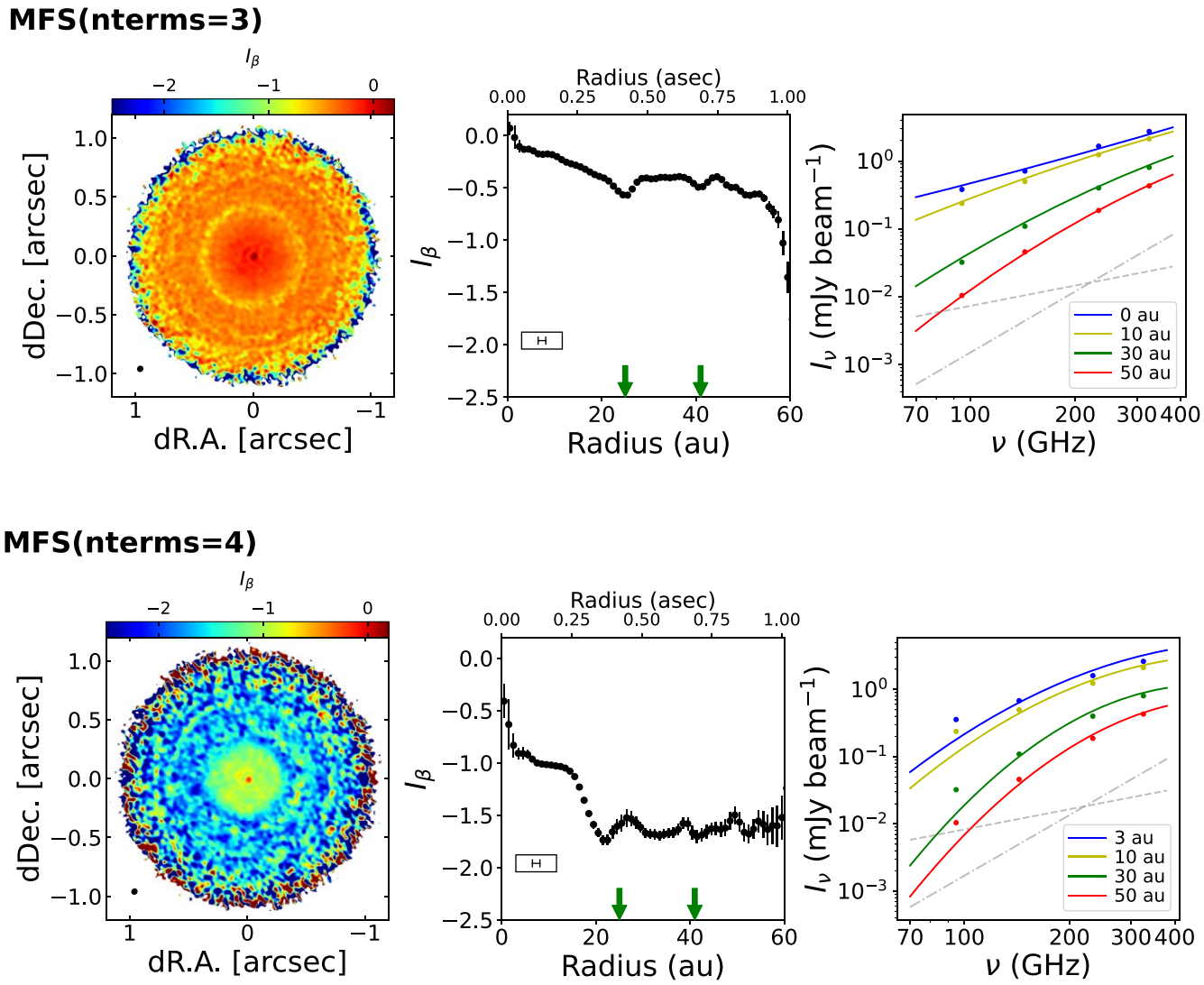

Figure 4. The distributions of the spectral curvature I_β and the inferred submillimeter spectrum for the cases of *nterms* = 3 and 4 in the upper and lower panels, respectively. Left: map of I_β reconstructed using the MFS method. The black circle in the bottom left corner denotes the beam size. Middle: deprojected and azimuthally averaged profile of I_β. The error bars represent the standard error of the azimuthal averaging. The bar in the box in the bottom left corner shows the geometric mean of the beam size. The green arrows in all the panels indicate the positions of the 25 and 41 au gaps, respectively. Right: the submillimeter spectra inferred from the I_α and I_β profiles, reconstructed with MFS. The azimuthally averaged spectra at 10, 30, and 50 au are shown in blue, orange, and green, respectively. The black dots indicate the flux densities measured in each band map. The dashed and dashed–dotted lines in gray show the ν^2 and ν^3 dependence, respectively, as a reference.

the residual of the sidelobe pattern. Another emission feature is that the emission ring at 45 au contains azimuthal wiggles, while dust wiggles are not present at the 33 au ring and 25 au gap. This indicates that the 45 au ring has nonzero eccentricity or that the center of the ring orbit is slightly different to that for the inner rings/gaps. Alternatively, the inner and outer disks might not be coplanar, or there might be an azimuthal variation of the ring's scale height (Doi & Kataoka 2021). These emission features will be confirmed and discussed through future observations and more detailed analysis.

4. Validation of the Imaging Methods Using Intensity Models

Our results indicate that for the MFS imaging, a higher-order Taylor expansion is required to reconstruct a reliable I_α map from data sets with wide frequency coverage at millimeter/submillimeter wavelengths. The higher orders of the Taylor expansion, however, require the data to have a significant S/N. On the other hand, although the resolution of the image is poorer than that of MFS, the image-oriented method provides an I_α map without using the Taylor series approximation for the frequency dependence.

In this section, we investigate the behavior of the MFS method by using an intensity model to validate the reconstructed spectral index maps. The intensity model is motivated by the intensity distribution of the TW Hya disk. The combined intensity and I_α maps were created using the same procedure as for the observed data. We compare them to determine which is the more reliable procedure for making the I_α map from data sets with a wide frequency coverage. Note that, for simplicity, we ignore the frequency dependence of the spectral slope, i.e., the spectral curvature.

The intensity model was assumed to be an exponential function, as described by $I = 1.7 \times 10^{-0.02R}$ mJy beam^{-1} at a representative frequency, i.e., the central frequency

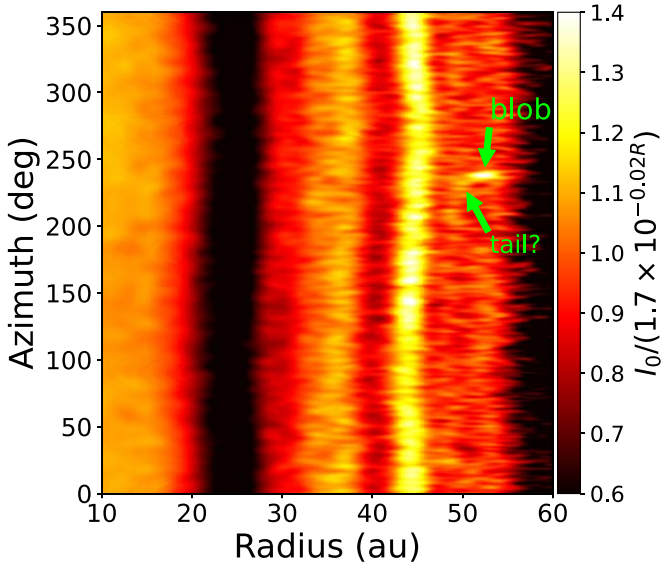

Figure 5. Intensity map of MFS *nterms* = 3 deprojected onto polar coordinates. The intensity scale is divided by $1.7\times10^{-0.02R}$ mJy beam^{-1} to clearly view the features embedded in the background emission of the protoplanetary disk (see Section 4). The millimeter blob emission reported by Tsukagoshi et al. (2019) and a candidate trailing tail found in this study are labeled.

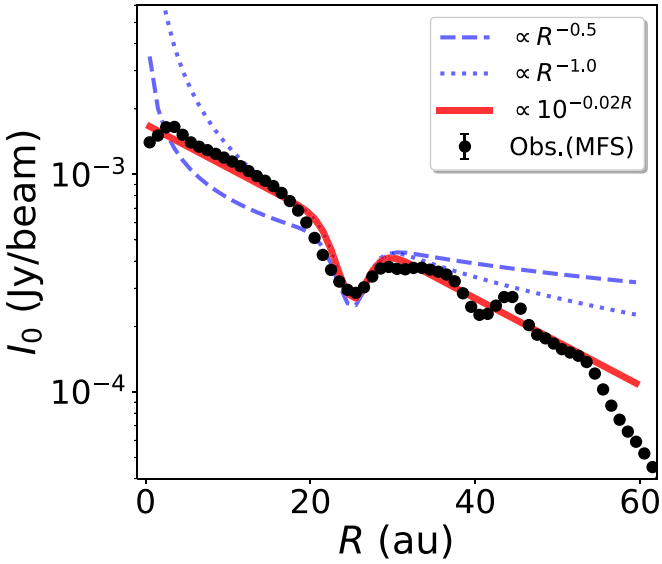

Figure 6. Comparison of the model intensity profile (red) to that of the observations (black dots). The radial profile of the combined intensity map reconstructed by MFS with *nterms* = 3 is adopted for the observed profile. The blue lines show a standard power-law form with R^{-p} dependence.

(∼221 GHz). The intensity profile was truncated at 1 and 60 au for the inner and outer radii, respectively. We also added an intensity gap at 25 au to the model profile to more closely resemble that of the TW Hya disk. The gap is modeled using a Gaussian function with an FWHM of 5 au and a fractional depth of 0.5. Figure 6 shows the comparison of the adopted intensity distribution and the observed intensity. The intensity profile of the model is more similar to the observed profile than the standard power-law dependence ($I \propto R^{-p}$).

We assumed three cases for the radial dependence of the spectral index $I_\alpha(R)$. The first one was a constant over the disk with a value of 2.5. The second one was a linear dependence with disk radius, in which $I_\alpha = 2$ at 10 au and 3.0 at 50 au were assumed. Finally, we adopted the linear dependence assumed above with an enhancement at the 25 au gap. The enhancement had a Gaussian form with the same width as the intensity gap (5 au in FWHM). The peak value of I_α enhancement was set to be 3.

Under these assumptions, model images were created at the same frequency sampling as the observed data sets. The model images were converted to visibilities and resampled to match each of the observations. The visibilities were resampled using the Python code *vis_sample*[14] (Loomis et al. 2017). Then, the model visibilities were imaged with the same parameters as for the observed data sets using the *tclean* task of CASA.

Figures 7–9 compare the simulated images reconstructed from the model visibilities. The reconstructed images of the intensity, spectral index, and their radial profiles are shown from left to right, respectively. The results of the image-oriented method and of MFS with *nterms* = 2, 3, and 4 are displayed from top to bottom. We summarize the results of the imaging tests below.

1. As mentioned in Section 2, the first order of the Taylor expansion (*nterms* = 2) cannot reproduce the spectrum between Bands 4 and 7. The simulated I_α is ∼20% lower than the input value for both the I_α models. The intensity of the combined map is also affected. By adopting the first order of the Taylor expansion for the MFS imaging, the intensity at the central frequency tends to be overestimated by 20%–40% (see Figure 3).
2. Following the abovementioned case, the MFS imaging that adopts *nterms* = 3 and 4 reasonably reproduces the I_α profile, not only for the constant I_α case, but also for the structured I_α cases. The difference between the mean I_α and the input value was typically less than 5%. In addition, there appear to be artificial ripples over the disk with a spatial scale of ∼10 au, seen particularly in the case of *nterms* = 3. Because the peak positions of the ripples vary if we adopt different multiscale parameters in CLEAN, the ripples could be caused by the combination of scale parameters.
3. Despite the difference in the I_α maps, the combined intensity is not significantly affected when *nterms* = 3 or 4 is adopted. In all of the I_α model cases, the difference between the peak intensities of *nterms* = 3 and 4 is less than 5%, indicating that both profiles describe the radial distribution of the disk emission well.
4. In both of the imaging methods, the existence of the intensity gap does not significantly affect the I_α profile. If we adopt *nterms* = 3 and 4, only a <2% variation around the 25 au gap is found when the linear dependence of I_α is the case. If there is an enhancement of I_α at the gap, the peak value of I_α is underestimated. However, the difference is as small as ∼10%. Beam smearing could also be a reason for the decrease in I_α in the image-oriented method.
5. The image-oriented method is a good method for reproducing a reliable I_α map, although image resolution is sacrificed. The radial dependence of I_α agrees reasonably well with the input dependence of I_α, and the noise level is significantly lower than that of higher-order MFS images. One concern is that in all of the I_α model cases, the values of the simulated I_α profiles are slightly larger

[14] https://github.com/AstroChem/vis_sample

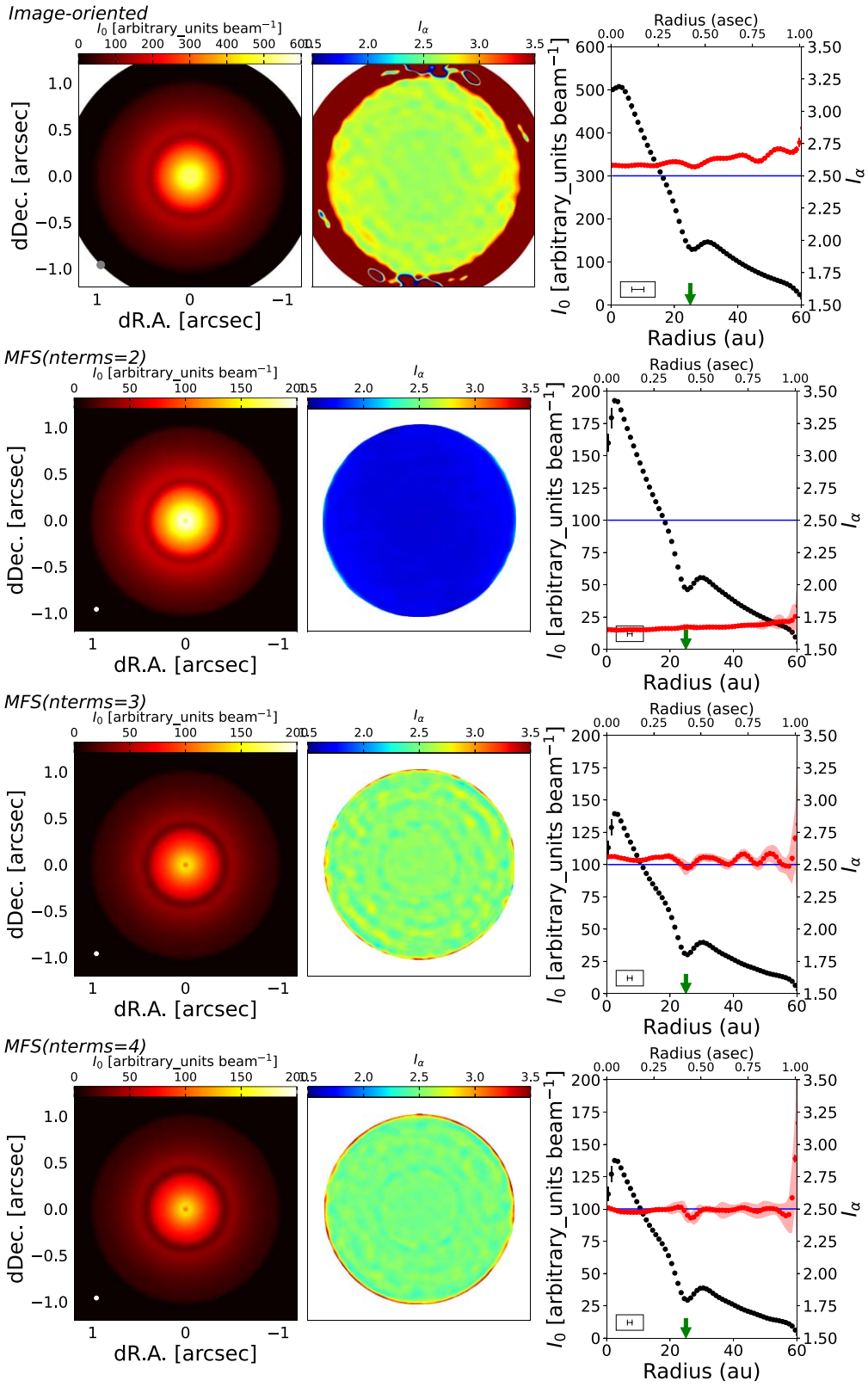

Figure 7. Comparison of the reconstructed images and radial distributions from the simulated visibilities using the image-oriented analysis (top) and the MFS method (from the second to bottom rows). The figure description is the same as that for Figure 2. The intensity scale is in arbitrary units. The results for the constant I_α model are shown. The green arrow indicates the gap position in the model profile. The blue line represents the model I_α profile.

than the model ($\lesssim$6%). This could be caused by the imaging of each band's intensity without using MFS, because the bandwidth ratio of each type of data is not negligible. Alternatively, how deep we take the clean components to make each band's image may also affect the spectral index map.

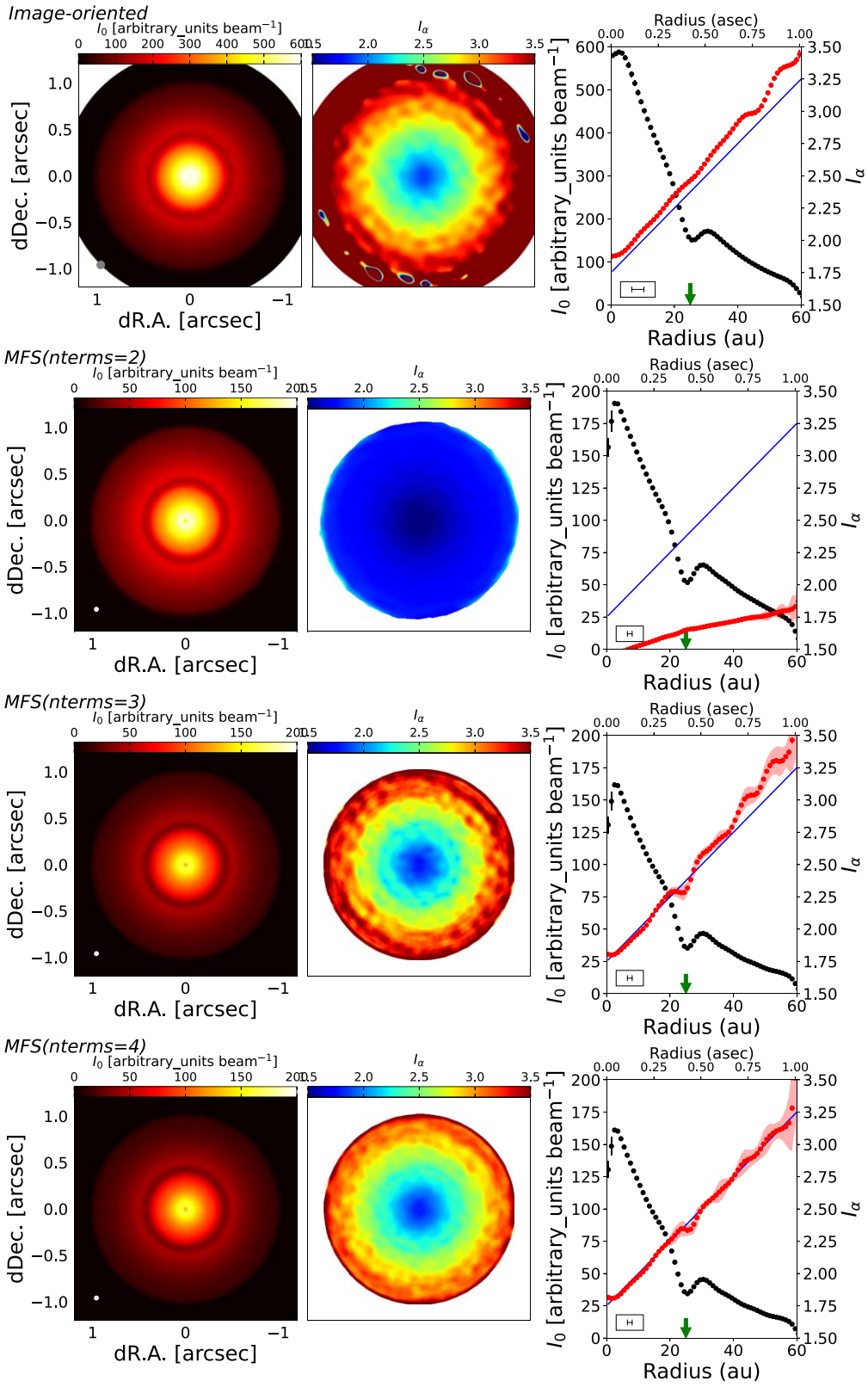

Figure 8. The same as Figure 7, but for the gradient I_α model.

Based on these results, we conclude that MFS with the second order of the Taylor expansion (*nterms* = 3) is a reasonable method for creating a high-resolution combined intensity map. This is because *nterms* = 2 cannot reproduce the flux density correctly, because of the wide frequency coverage, and *nterms* = 4 or higher causes difficulty in reconstructing the spectral curvature. Although *nterms* = 4 can provide a spectral slope comparable to or better than *nterms* = 3, the number of Taylor coefficients is larger than the number of parameters required for describing a submillimeter spectrum (I_0, I_α, and

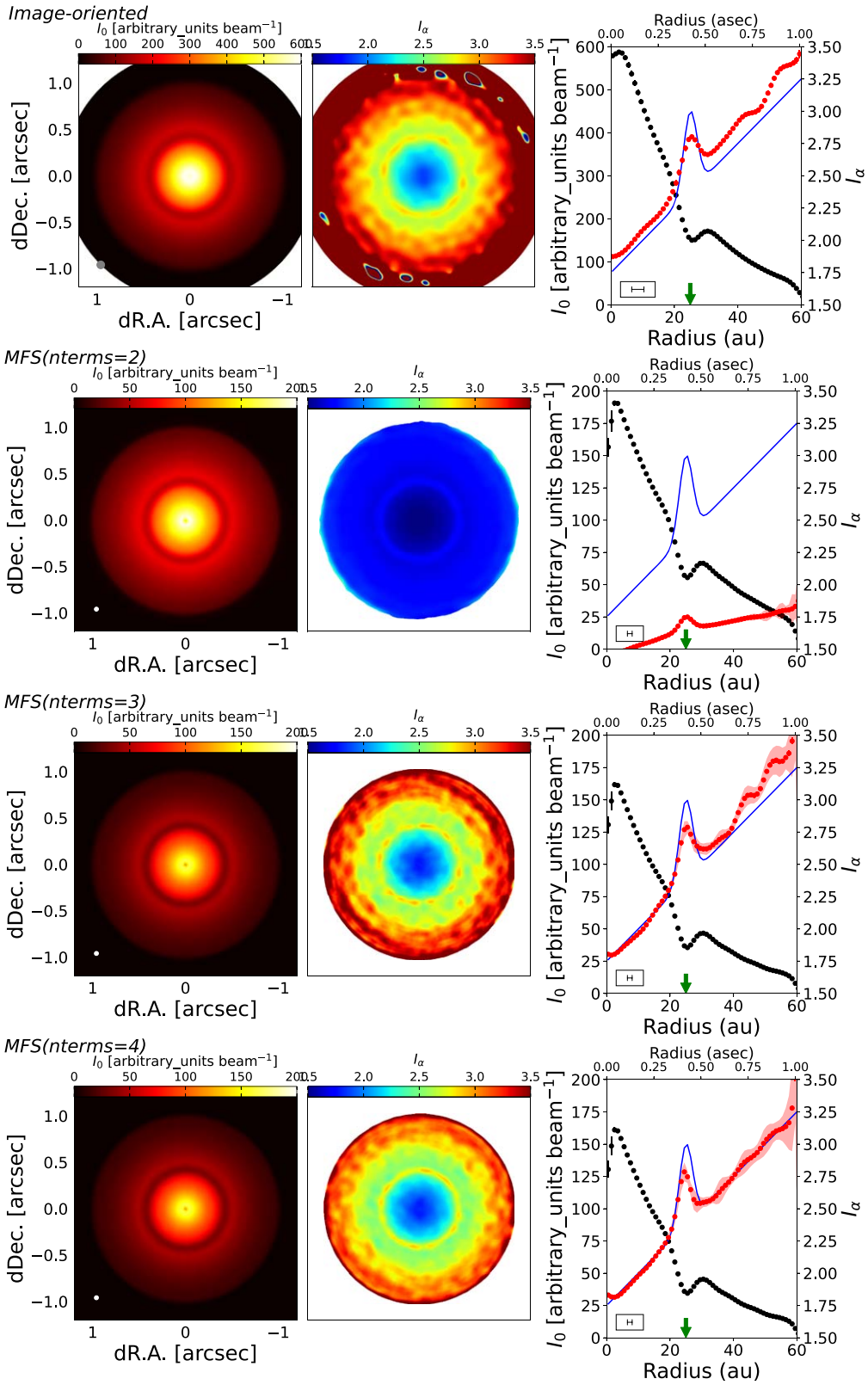

Figure 9. The same as Figure 7, but for the model of the gradient I_α with an enhancement at 25 au.

I_β), as shown in Section 3. The artifact of the I_α profile associated with the intensity gaps is negligible. However, if I_α is enhanced at the gap, the peak value is underestimated by $\sim$10%. Although the resolution is lower than that of the MFS images, the image-oriented method provides a more robust I_α map. The uncertainty owing to the selection of the imaging method is expected to be $\lesssim$10% if the spectral curvature is negligible. Thus, we conclude that the imaging method is reliable in checking both the I_α images reconstructed from MFS (*nterms* = 3) and the image-oriented method.

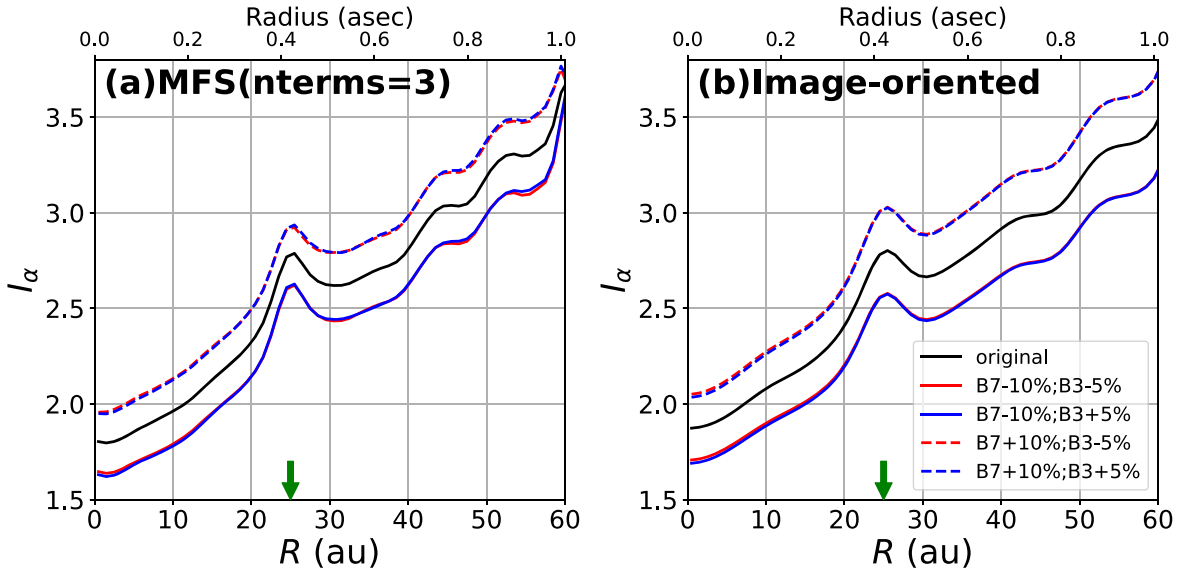

Figure 10. Reconstructed I_α profiles simulated by adding the modulation of the flux density scale. The cases of +10% and −10% flux density modulation at Band 7 are shown with the solid and dashed lines, respectively, and the cases of +5% and −5% modulation at Band 3 are shown with the blue and red lines, respectively. The original profile, without flux density modulation, is shown in black. The green arrow indicates the gap position in the model profile. The results for (a) MFS (*nterms* = 3) and (b) the image-oriented method are shown.

Finally, we checked how the uncertainty in the absolute flux density calibration affects the I_α profile by using the same procedure as the mock observation for the intensity model. We employed an intensity model whose spectral index increases linearly with radius, with an enhancement at the gap. To observe the effect of the absolute flux calibration uncertainty on the reconstructed spectral slope, we ran mock observations for four cases, in which the flux density of the model profile was modified by ±10% at Band 7 and ±5% at Band 3, keeping the original I_α profile. The flux densities at Bands 4 and 6 were unchanged.

Figure 10 shows the results of the reconstructed radial profile of I_α using MFS (*nterms* = 3) and the image-oriented method. It is clear that the uncertainty of the flux calibration does not affect the shape of the I_α profile, but that it does affect the value of I_α. Moreover, the value of I_α is more dependent on the uncertainty of the Band 7 flux calibration than that of Band 3. The differences to the original profile are typically 7% for the MFS method and 8% for the image-oriented method. Note that this is a conservative technique for determining the uncertainty due to the absolute flux calibration because we combine multiple measurement sets for each band. Thus, the uncertainty of the absolute flux calibration should be lower than those reported by ALMA (10% for Band 7 and 5% for Band 3).

5. Discussion

5.1. Comparison with the Spectral Index Distribution of Macias et al. (2021)

With I_0, I_α, and I_β derived with MFS *nterms* = 3 (see Figures 2 and 4), we can describe the submillimeter spectrum using Equation (1) and measure the spectral slope α_ν at a specific frequency. Figure 11 shows the derived α_ν at frequencies of 121, 190, and 290 GHz, which correspond to the central frequencies between ALMA Band 3 and 4 (Band3+4), 4 and 6 (Band4+6), and 6 and 7 (Band6+7), respectively. The overall trend is that α_ν decreases as the frequency increases. This trend is more prominent at $\gtrsim$20 au; α_ν decreases to values of ∼0.5, from 121 to 290 GHz, and ∼0.2, near 10 au, respectively. The enhancements of α_ν at the intensity gaps (25 and 43 au) appear in all α_ν cases, and their excess compared to the surroundings decreases as the frequency increases. As the spectral index determined by the image-oriented method using data from all of the bands is independent of the frequency, it seems to agree with the profile for the Band3+4 case, but cannot describe the profile for the Band6+7 case. If we make α_ν profiles of the image-oriented method using band-to-band fitting, the same trend in frequency as the MFS profiles is found, although they have larger uncertainty.

Recently, Macias et al. (2021) presented the distribution of α_ν for the TW Hya disk at a resolution of 50 mas. The difference from our study is that they measured α_ν between Bands 3–4, 4–6, and 6–7 separately, by using MFS *nterms* = 2, while our study focuses on determining I_α and I_β through the MFS *nterms* = 3 imaging. Figure 11 also compares our results of α_ν with those derived by Macias et al. (2021). Our α_ν profiles can reproduce the frequency dependence of Macias et al. (2021). The radial variation of the profiles is also almost consistent. However, there is still a discrepancy in the excess in α_ν at the intensity gaps; the results of Macias et al. (2021) show that the excess of α_ν at the gaps is largest at Bands 6 and 7, whereas our result shows the opposite trend. This is probably because our α_ν measurement, by combining data over four bands, improves the S/N of the profile.

5.2. Implication of the Dust Size Distribution

In this subsection, we deduce the optical depth τ_0 at the central frequency ν_0, the power-law index of the dust opacity β, and the temperature of the dust disk T_d using the submillimeter spectrum derived from our MFS imaging. If we neglect the scattering of dust, the intensity of the dust emission I_ν is expressed as

$$I_\nu = B(T_d)\left[1 - \exp\left\{-\tau_0\left(\frac{\nu}{\nu_0}\right)^\beta\right\}\right], \quad (4)$$

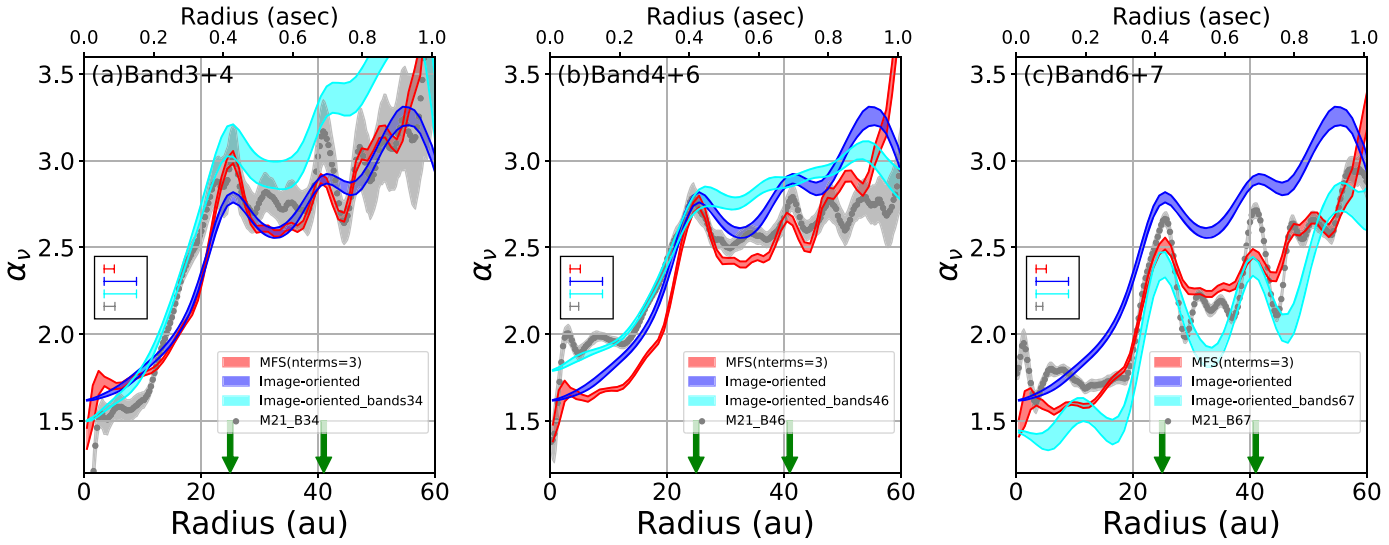

Figure 11. The radial profile of the spectral slope α_ν for the case of MFS (*nterms* = 3) is shown in red. The profiles at the frequencies between Bands 3 and 4 (Band3+4; 121 GHz), Bands 4 and 6 (Band4+6;190 GHz), and Bands 6 and 7 (Band6+7; 290 GHz) are shown in (a)–(c), respectively. The α_ν profile determined by the image-oriented method using data from all bands is shown in blue, while those derived from the band-to-band fitting are shown in cyan. The shaded area indicates the standard error. The green arrows indicate the positions of the 25 and 41 au gaps. For reference, the radial profiles of the spectral index measured in Macias et al. (2021) are shown by the gray dots. The bars in the box represent the beam sizes of the profiles.

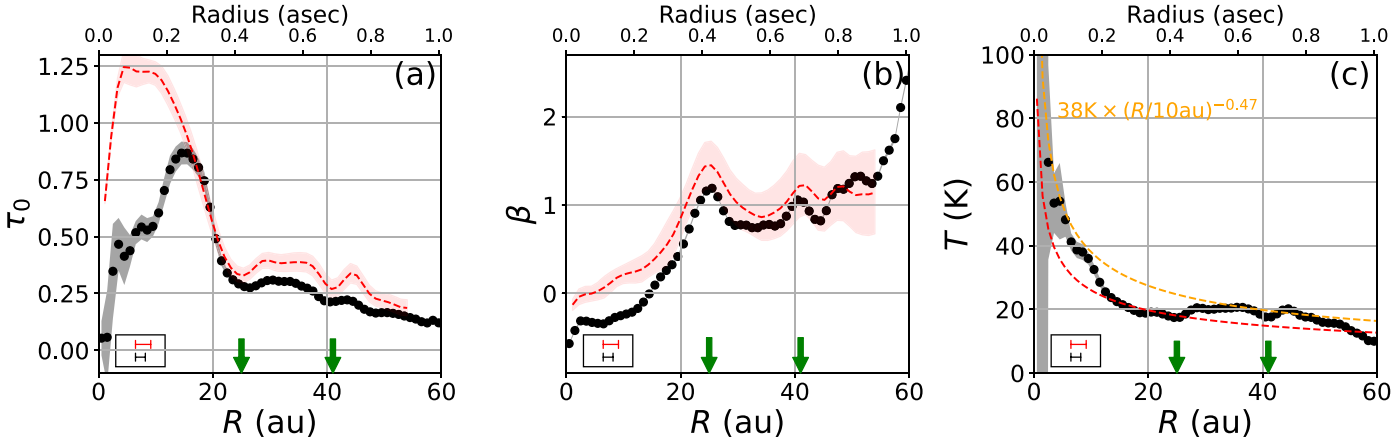

Figure 12. Radial profiles of the optical depth at 221 GHz τ_0 (a); power-law index of the opacity coefficient β (b); and the temperature of the dust disk T_d (c). The profiles are calculated based on the maps reconstructed by MFS *nterms* = 3. The shaded region corresponds to the minimization error. As a reference in (a) and (b), τ and β at 190 GHz derived by Tsukagoshi et al. (2016) are shown by the dashed red line, with the shaded region showing the standard error (T_{10} = 26 K and $q = -0.4$ case). In (c), the disk midplane temperature profiles assumed in Tsukagoshi et al. (2016) and derived by Zhang et al. (2017) are indicated by the red and yellow dashed lines, respectively. The green arrows in all of the panels indicate the positions of the 25 and 41 au gaps. The mean beam sizes of this study and those of Tsukagoshi et al. (2016) are shown by the bars in black and red, respectively, in the bottom left corner of each panel.

where $B(T_d)$ is the Planck function. There are three unknown variables, τ_0, β, and T_d, in this equation. On the other hand, the observed submillimeter intensity, I_ν(obs), can be expressed using three parameters determined by our MFS imaging, I_{ν_0}, I_α, and I_β, as

$$I_\nu(\mathrm{obs}) = I_{\nu_0}\left(\frac{\nu}{\nu_0}\right)^{I_\alpha + I_\beta \log\left(\frac{\nu}{\nu_0}\right)}. \quad (5)$$

This implies that we can solve the unknown three variables from the submillimeter spectrum.

To address this problem, we calculated the minimization of $\Delta I_\nu \equiv I_\nu - I_\nu$(obs) by varying τ_0, β, and T_d. We used *curve_fit* in the *scipy* optimization module to minimize ΔI_ν. To prevent divergence, the solution was searched for with minimum and maximum bounds of 0.001–10, −3–3, and 10–300 for τ_0, β, and T_d, respectively. The standard errors in the radial profiles of the observed parameters were used to determine the weight of the minimization.

The derived profiles of τ_0, β, and T_d are shown in Figure 12. The disk is entirely optically thin at 221 GHz, although only marginally so at ∼15 au. The shape of the τ_0 profile is consistent with that obtained in Tsukagoshi et al. (2016) at >15 au, but it deviates at the inner radii, mainly due to the difference in the disk temperature profiles adopted. As shown in Figure 12(c), our direct measurement of the dust temperature T_d agrees well with the estimate obtained by a modeling approach for the gas disk (Zhang et al. 2017).

The radial dependence of β is similar to that derived in Tsukagoshi et al. (2016). The value is slightly smaller (∼0.1–0.3) than that derived in Tsukagoshi et al. (2016), probably because of the difference of the frequency range over which β was determined. The enhancements of β associated with the 25 and 41 au gaps are also seen. This result still

supports the conclusion of Tsukagoshi et al. (2016), which is that this can be explained by a deficit of millimeter-sized grains within the gap. In the inner region of the disk ($R \lesssim 15$ au), where the effect of the optical depth cannot be ignored, β is less than 0; this indicates that the emission is blackbody-like, or that the scattering of millimeter radiation is effective (Liu 2019; Ueda et al. 2020). The scattering should be responsible for a difference of approximately one order of magnitude between our estimate of the optical depth and that derived by Macias et al. (2021).

According to theoretical predictions of the dust opacity (e.g., Birnstiel et al. 2018), $\beta \sim 1$ implies that the power-law index of the dust size distribution q is $\sim$3.5 and that the maximum dust particle size is above 1 mm. Beyond the 25 au gap, where the emission is optically thin, β varies up to $\sim$1.5 at 60 au, meaning that the maximum dust size could be a few millimeters.

This conclusion is supported by the detailed modeling of the dust size distribution for sets of high-resolution ALMA data (Macias et al. 2021). Note that, in our study, the disk parameters are determined from optically thinner frequency bands (Bands 3, 4, 6, and 7). By adding optically thick continuum data at higher-frequency bands (Bands 9 or 10), the disk parameters, particularly the dust temperature profile, can be determined more robustly (Kim et al. 2019).

6. Summary

To obtain a higher-sensitivity intensity map at millimeter wavelengths and to revisit the dust size distribution of the protoplanetary disk around TW Hya, we created high-resolution maps of the intensity and the spectral index by combining sets of ALMA data at Bands 3, 4, 6, and 7. In addition to using the existing ALMA archive data, we have newly conducted high-resolution observations at Bands 4 and 6, some of which have already been published in Tsukagoshi et al. (2019). Two methods are employed to reconstruct the combined intensity and the spectral index maps; a traditional image-oriented method and multiscale MFS. The impacts resulting from the choice of method were also investigated using an intensity model motivated by TW Hya. The results of this paper are summarized as follows:

1. We show the spectral index maps reconstructed with both imaging methods. A reasonable method for reconstructing the spectral index map is MFS with the second order of the Taylor expansion for the frequency ($nterms = 3$). With a smaller order of the Taylor expansion ($nterms = 2$), the number of Taylor coefficients is too small to reproduce the frequency dependence from Bands 3 to 7. Meanwhile, the higher-order ($nterms = 4$) MFS imaging requires a larger number of Taylor coefficients and a higher S/N. Although the resolution is almost twice as poor, the image-oriented method provides a consistent spectral index map with MFS ($nterms = 3$) imaging.
2. The spectral index reconstructed with MFS $nterms = 3$ agrees well with that derived in previous studies (Tsukagoshi et al. 2016; Huang et al. 2018; Macias et al. 2021). The index decreases toward the disk center and shows enhancements in the intensity gaps. The spectral index of the image-oriented method showed similar structures. Our MFS $nterms = 3$ imaging shows that the submillimeter spectrum of TW Hya has spectral curvature, indicating that the spectral index depends on the frequency.
3. We investigated how the substructures of intensity distribution affect the reconstructed spectral index map by using an intensity model and noise-free mock observations. We validated that the first order of the Taylor expansion is insufficient for reproducing the frequency dependence from Bands 3 to 7, and that the higher-order Taylor expansion of MFS ($nterms = 3$ and 4) is necessary. We found that the higher-order MFS method can provide a high-resolution spectral index distribution with an uncertainty of $<10\%$, and that the presence of the intensity gap does not significantly influence the reconstruction of the spectral index distribution. Although the resolution is lower than that of the MFS images, the image-oriented method also provides a robust distribution of the spectral index, if there is no frequency dependence in the spectral index.
4. We formulated the submillimeter spectrum of the TW Hya disk as a function of the disk radius by using the images reconstructed with MFS $nterms = 3$. With the spectrum, the optical depth τ_0, the power-law index of the opacity coefficient β, and the temperature of the dust disk T_d were derived under the assumption that scattering is negligible. The derived τ_0 and β agree well with those derived in our previous work (Tsukagoshi et al. 2016). The enhancement of β at the intensity gaps was also confirmed, supporting a deficit of millimeter-sized grains within the gap.
5. By combining all of the visibilities from Bands 3 to 7, we made the highest-sensitivity continuum map at millimeter wavelengths to date. The point-source sensitivity of our map was improved by 30% from the previous highest-sensitivity continuum map of Tsukagoshi et al. (2019). The previously reported substructures in the dust emission were confirmed by our maps. The tentative detection of a new emission feature associated with the millimeter blob has also been reported, but it should be confirmed by future observations and detailed analysis.

We would like to thank the referee for improving our manuscript. We are also grateful to Enrique Macias for sharing the spectral index profiles of the TW Hya disk. This paper makes use of the following ALMA data: ADS/JAO.ALMA#2013.1.00114.S, 2013.1.00387.S, 2015.A.00005.S, 2015.1.00308.S, 2015.1.00686.S, 2015.1.00845.S, 2016.1.00229.S, 2016.1.00311.S, 2016.1.00440.S, 2016.1.00464.S, 2016.1.00629.S, 2016.1.00842.S, 2016.1.01495.S, 2017.1.00520.S, and 2018.1.01218.S. ALMA is a partnership of ESO (representing its member states), NSF (USA), and NINS (Japan), together with NRC (Canada), MOST and ASIAA (Taiwan), and KASI (Republic of Korea), in cooperation with the Republic of Chile. The Joint ALMA Observatory is operated by ESO, AUI/NRAO, and NAOJ. A part of the data analysis was carried out on the common-use data analysis computer system at the Astronomy Data Center of NAOJ. This work was supported by JSPS KAKENHI grant Nos. 17K14244, 18H05438, and 20K04017. C.W. acknowledges financial support from the University of Leeds, the Science and Technology Facilities Council, and UK Research and Innovation (grant Nos. ST/T000287/1 and MR/T040726/1). T.J.M. thanks the STFC for support via grants ST/P000312/1 and ST/T000198/1. M.T. was supported by JSPS KAKENHI grant Nos. 18H05442,

15H02063, and 22000005. K.D.K was supported by JSPS KAKENHI grant No. 19K14779.

Facility: ALMA.

Software: CASA (McMullin et al. 2007), numpy (Harris et al. 2020), scipy (Virtanen et al. 2020), astropy (Astropy Collaboration et al. 2013), matplotlib (Hunter 2007), vis_sample (Loomis et al. 2017).

ORCID iDs

Takashi Tsukagoshi https://orcid.org/0000-0002-6034-2892
Hideko Nomura https://orcid.org/0000-0002-7058-7682
Ryohei Kawabe https://orcid.org/0000-0002-8049-7525
Kazuhiro D. Kanagawa https://orcid.org/0000-0001-7235-2417
Satoshi Okuzumi https://orcid.org/0000-0002-1886-0880
Shigeru Ida https://orcid.org/0000-0001-9564-6186
Catherine Walsh https://orcid.org/0000-0001-6078-786X
Tom J. Millar https://orcid.org/0000-0001-5178-3656
Sanemichi Z. Takahashi https://orcid.org/0000-0003-3038-364X
Jun Hashimoto https://orcid.org/0000-0002-3053-3575
Taichi Uyama https://orcid.org/0000-0002-6879-3030
Motohide Tamura https://orcid.org/0000-0002-6510-0681

References

Akiyama, E., Muto, T., Kusakabe, N., et al. 2015, ApJL, 802, L17
ALMA Partnership, Brogan, C. L., Pérez, L. M., et al. 2015, ApJL, 808, L3
Andrews, S. M., Huang, J., Pérez, L. M., et al. 2018, ApJL, 869, L41
Andrews, S. M., Wilner, D. J., Zhu, Z., et al. 2016, ApJL, 820, L40
Astropy Collaboration, Robitaille, T. P., Tollerud, E. J., et al. 2013, A&A, 558, A33
Banzatti, A., Pinilla, P., Ricci, L., et al. 2015, ApJL, 815, L15
Birnstiel, T., Dullemond, C. P., Zhu, Z., et al. 2018, ApJL, 869, L45
Debes, J. H., Poteet, C. A., Jang-Condell, H., et al. 2017, ApJ, 835, 205
Dent, W. R. F., Pinte, C., Cortes, P. C., et al. 2019, MNRAS, 482, L29
Doi, K., & Kataoka, A. 2021, ApJ, 912, 164
Dullemond, C. P., & Dominik, C. 2005, A&A, 434, 971
Gaia Collaboration, Brown, A. G. A., Vallenari, A., et al. 2016, A&A, 595, A2
Harris, C. R., Millman, K. J., van der Walt, S. J., et al. 2020, Natur, 585, 357
Hayashi, C. 1981, PThPS, 70, 35
Huang, J., Andrews, S. M., Cleeves, L. I., et al. 2018, ApJ, 852, 122
Huang, J., Andrews, S. M., Dullemond, C. P., et al. 2020, ApJ, 891, 48
Hunter, J. D. 2007, CSE, 9, 90
Isella, A., Benisty, M., Teague, R., et al. 2019, ApJL, 879, L25
Kim, S., Nomura, H., Tsukagoshi, T., Kawabe, R., & Muto, T. 2019, ApJ, 872, 179
Liu, H. B. 2019, ApJL, 877, L22
Long, F., Pinilla, P., Herczeg, G. J., et al. 2020, ApJ, 898, 36
Loomis, R. A., Öberg, K. I., Andrews, S. M., & MacGregor, M. A. 2017, ApJ, 840, 23
Macias, E., Guerra-Alvarado, O., Carrasco-Gonzalez, C., et al. 2021, A&A, 648, A33
McMullin, J. P., Waters, B., Schiebel, D., Young, W., & Golap, K. 2007, in ASP Conf. Ser. 376, Astronomical Data Analysis Software and Systems XVI, ed. R. A. Shaw, F. Hill, & D. J. Bell (San Francisco, CA: ASP), 127
Miyake, K., & Nakagawa, Y. 1993, Icar, 106, 20
Nayakshin, S., Tsukagoshi, T., Hall, C., et al. 2020, MNRAS, 495, 285
Pascucci, I., Gorti, U., & Hollenbach, D. 2012, ApJL, 751, L42
Qi, C., Ho, P. T. P., Wilner, D. J., et al. 2004, ApJL, 616, L11
Rau, U., & Cornwell, T. J. 2011, A&A, 532, A71
Teague, R., Bae, J., Huang, J., & Bergin, E. A. 2019, ApJL, 884, L56
Tsukagoshi, T., Muto, T., Nomura, H., et al. 2019, ApJL, 878, L8
Tsukagoshi, T., Nomura, H., Muto, T., et al. 2016, ApJL, 829, L35
Ueda, T., Kataoka, A., & Tsukagoshi, T. 2020, ApJ, 893, 125
van Boekel, R., Henning, T., Menu, J., et al. 2017, ApJ, 837, 132
Virtanen, P., Gommers, R., Oliphant, T. E., et al. 2020, NatMe, 17, 261
Zhang, K., Bergin, E. A., Blake, G. A., Cleeves, L. I., & Schwarz, K. R. 2017, NatAs, 1, 0130
Zhu, Z., Nelson, R. P., Dong, R., Espaillat, C., & Hartmann, L. 2012, ApJ, 755, 6